Prediction of Scattered Fine-Scale Jet Mixing Noise using Lilley's Acoustic Analogy

Alexander N. Carr* and Steven A. E. Miller†
University of Florida, Gainesville, Florida, 32611-6250

The fine-scale mixing noise model of Tam and Auriault is formulated in the context of Lilley's acoustic analogy. The solution for the spectral density of fine-scale mixing noise at a given observer location is shown to be an integral of the source terms and a modified Green's function over the volume of the jet plume. The modified Green's function is the solution to Lilley's equation subject to derivative operations resulting from the re-arrangement of the convolution with the source term. Two different modified Green's functions are implemented. The first Green's function ($\mathcal{G}_0$) is computed assuming no mean flow refraction effects. The second Green's function ($\mathcal{G}_q$) is a high frequency asymptotic solution to Lilley's equation. Both Green's functions are shown to scale with Mach number for three subsonic jet Mach numbers, with $\mathcal{G}_q$ showing improved spectral predictions at high frequencies. The effects of shielding by a semi-infinite flat plate are examined through the use of two tailored Green's functions. For a $M = 0.985$ cold jet, the tailored $\mathcal{G}_q$ improves ΔdB predictions for observer angles $\theta \geq 100°$.

Nomenclature

Symbols	Description
c	Speed of sound
c_l	Turbulent length scale empirical constant
c_q	Fine-scale turbulent pressure empirical constant
c_τ	Turbulent time scale empirical constant
D	Nozzle exit diameter
G	Green's function of Lilley's equation in frequency domain
$\mathcal{G}$	First modified Green's function $\mathcal{G} = \nabla_s \cdot \bar{c}_s^2 \nabla_s G$
$\mathbb{G}$	Second modified Green's function
g	Green's fn of Lilley's Eqn. in time domain
$\hat{g}$	Green's fn of Lilley's Eqn. in frequency domain $\hat{g} = Ge^{i\omega t_s}$
k	Turbulent kinetic energy $1/2\langle u'u' \rangle$
l_s	Fine-scale turbulent length scale
M_d	Design Mach number
M_j	Jet exit Mach number $M_j = u_j/c$
p	Pressure
p_{ref}	Acoustic reference pressure in air $p_{ref} = 2 \times 10^{-5}$
q	Fine-scale turbulent pressure
$\hat{q}_s$	Fine-scale turbulent pressure adjusted by constant
r	Radial coordinate of the jet
t	Observer time
t_s	Source time
u	Velocity
u_j	Jet exit velocity
x	Coordinate aligned with the axis of the jet
$\mathbf{x}$	Observer vector
$\mathbf{x}_s$	Source vector
y	Coordinate orthogonal to x in the vertical direction
z	Coordinate orthogonal to x and y
$\langle\rangle$	Ensemble averaging

Greek Symbols	
β	Azimuthal angle in plate coordinates
Γ	Material derivative of fine-scale turbulent pressure Dq_s/Dt
Γ_q	Fine-scale turbulent pressure q_s
γ	Ratio of specific heats
δ	Dirac delta function
δ_{ij}	Kronecker delta function
δ_s	Shear layer thickness
ϵ	Turbulent dissipation rate
ζ	Seperation distance in the z-direction
η	Seperation distance in the y-direction
$\boldsymbol{\eta}$	Seperation vector
θ	Observer polar angle measured from downstream axis
κ	Acoustic wavenumber ωc_∞^{-1}
Λ	Source of fine-scale mixing noise in Lilley's acoustic analogy
λ	Acoustic wavelength
ξ	Seperation distance in the x-direction
ρ	Density
ϱ	Radial distance in plate coordinates
τ	Delayed time
τ_s	Fine-scale turbulent time scale
τ_{ij}	Shear stress
ϕ	Azimuthal angle
ω	Radial frequency
ω_t	Specific dissipation rate

Non-Dimensional Numbers	
M	Mach number
St	Strouhal number $\mathrm{St} = fD/u_j$

Abbreviations	
BEM	Boundary Element Method
CFD	Computational Fluid Dynamics
FastBEM	Fast Boundary Element Method code
LES	Large-Eddy Simulation
NPR	Nozzle Pressure Ratio
OASPL	Overall Sound Pressure Level
RANS	Reynolds-averaged Navier-Stokes
SHJAR	Small Hot Jet Acoustic Rig
SST	Shear Stress Transport
TKE	Turbulent Kinetic Energy k
TTR	Total Temperature Ratio

Superscripts	
$\bar{}$	Reynolds average
$\tilde{}$	Favre average
$'$	Fluctuating quantity
$\hat{}$	Root mean square of quantity
*	Conjugation

Subscripts	
p	Denotes a quantity evaluated at the plate trailing edge location
s	Denotes a quantity evaluated at the source location (i.e. $f_s = f(\mathbf{x}_s)$)
∞	Denotes a quantity evaluated in the far-field (i.e. $f_\infty = \lim_{\mathbf{x}\to\infty} f(\mathbf{x})$)

*Ph.D. Student, Department of Mechanical and Aerospace Engineering, alexcarr.1721@gmail.com, AIAA student member.

†Assistant Professor of Mechanical and Aerospace Engineering, Department of Mechanical and Aerospace Engineering, University of Florida, 231 MAE-A, P. O. Box 116250, Gainesville, FL 32611, saem@ufl.edu; saemiller@gmail.com, AIAA Senior and lifetime member.

I. Introduction

The scattering of fine-scale mixing noise from turbulent jets contributes to the noise produced around civilian and military airfields. This noise has a direct impact on the perceived noise level of nearby workers and communities. On naval surface warships, jet noise is scattered by the ship deck and blast deflectors. For commercial aircraft, the sound field is scattered by geometry such as pylons and trailing edges. The intensity of jet noise causes hearing damage to nearby military personnel and is an annoyance to the surrounding community. In order to predict the scattering effects of jet noise by boundaries, previous approaches have implemented ray theory or numerical Green's function calculations to propagate the source noise from computational fluid dynamic (CFD) simulations. Even for simple scattering geometries, the calculation of the Green's function using a boundary element method (BEM) scheme can be prohibitively expensive. We seek to accurately capture both the refraction effects of the jet flow-field and the scattering of the jet fine-scale mixing noise in a new computationally efficient approach.

A. Previous Approaches

Jet noise suppression by shielding techniques have been studied in several experimental investigations. Balsa et al. [1] conducted a study of the shielding effects for a simple flat plate with a circular six tube cluster jet. Balsa et. al. [1] found that only high frequency sources close to the nozzle are shielded. Wang [2] conducted an experiment to study the effect of a model scale wing section above a jet. Wang [2] found that the high-frequency noise increased in the directions of reflection due to the wing. Brown [3] conducted jet-surface interaction tests of a plate underneath a circular jet, which mimics an aircraft wing used as a shield. The tests were conducted in the Small Hot Jet Acoustic Rig (SHJAR) at NASA for trailing edge locations that spanned $2 \leq xD^{-1} \leq 20$ and plate height locations spanning $1 \leq rD^{-1} \leq 16$, where x is the axial distance downstream from the nozzle exit, r is the radial distance from the jet centerline, and D is the nozzle exit diameter. This comprehensive test matrix provided acoustic shielding data for a broad range of engine-wing configurations. Brown [3] found that high-frequency noise incurred the most significant decrease in intensity from shielding effects, while the low frequency noise increased for plate positions that produced jet structure interaction noise.

Khavaran et al. [4] obtained predictions of jet mixing noise based on the methodology developed by Balsa et al. [1] in the "MGB" code. Khavaran et al. [4] used CFD computations with a $k-\epsilon$ turbulence model to simulate the jet flow, and adopted Lighthill's acoustic analogy to predict the noise. Zhao et al. [5] performed Large Eddy Simulations (LES) of subsonic turbulent jets and predicted the far-field noise with Kirchhoff's method. They found that the directivity of far-field noise was not uniform as predicted by Lighthill's theory, and there was a preferred radiation angle of the noise between 35 and 70 degrees from the downstream axis. Khalighi et al. [6] performed an unstructured LES simulation of different jet configurations. Khalighi et al. [6] obtained acoustic predictions through the use of a Ffowcs Williams and Hawkings [7] porous surface. The acoustic predictions of Khalighi et al. [6] compared favorably with experimental data for different jet configurations, including impinging jets.

Tam and Auriault [8] developed predictions for fine-scale turbulent mixing noise using the linearized Reynolds-averaged Navier-Stokes (RANS) equations. The source was modeled by using a comparison to the kinetic theory of gases as $q_s = (2/3)\rho k_s$, where ρ is the density and k_s is the kinetic energy of fine-scale turbulence. Tam and Auriault [8] used an adjoint Green's function to capture the effects of refraction by the jet. Morris and Farassat [9] compared existing acoustic analogy approaches to Tam and Auriault's [8] fine-scale prediction model. They argued that Tam and Auriault [8] obtain more favorable spectral predictions at sideline angles due to an improved source model. Morris and Farassat [9] then demonstrated that if consistent assumptions are made in modeling the source terms, both the acoustic analogy and Tam and Auriault's [8] model yield nearly identical predictions. Smith and Miller [10] analyzed the effects of acoustic attenuation in the sideline direction from the presence of a semi-infinite flat plate using Tam and Auriault's [8] fine-scale mixing noise model. Miller [11] used an acoustic analogy to predict the mixing noise of a jet in the presence of an infinite surface. The prediction used an approximate Green's function of Lilley's equation. This Green's function incorporated the Green's function of the convective Helmholtz equation, which in the presence of an infinite plane was evaluated with the method of images. Miller [12] later extended this prediction to include scattering effects from arbitrary surfaces using a ray theory method. Papamoschou [13] used a wavepacket approach to obtain shielding predictions of jet noise sources by a semi-infinite flat plate. The diffraction of sound around the semi-infinite flat plate was computed with a conventional BEM method and a fast multipole BEM (FastBEM) developed by Liu [14].

B. Present Approach

In the present approach, Tam and Auriault's [8] fine-scale mixing noise prediction model is rearranged in the form of Lilley's acoustic analogy. The far-field acoustic pressure is solved for through the convolution integral of the Green's function for Lilley's equation and the fine-scale turbulent source term. The pressure solution is then rearranged to recover the solution of Tam and Auriault [8] with a Green's function that is consistent with Lilley's acoustic analogy [15]. An additional term appears in the integral solution due to the acoustic analogy formulation. This additional term is negligible compared to the source term of Tam and Auriault [8].

Spectral density predictions for cold jets operating at $0.513 \leq M_j \leq 0.985$ are obtained. Predictions of the noise spectra in the sideline direction are compared to the experimental data of Brown and Bridges [16]. The predictions are calibrated for a jet operating at nozzle pressure ratio NPR = 1.861, total temperature ratio TTR = 1.00, and fully-expanded Mach number of $M_j = 0.9851$ at the sideline direction. The comparisons of spectral predictions and experimental data are evidence of the validity of Lilley's acoustic analogy to predict fine-scale mixing noise when Tam and Auriault's [8] source term is used.

Refraction effects are accounted for via the Green's function solution of Lilley's equation with a non-zero jet mean flow. Two different Green's functions are implemented to obtain predictions of the far-field noise spectrum for static jets. In the presence of a semi-infinite plate the Green's functions are modified to account for the boundary conditions on the plate. The first is a free-space Green's function solution to Lilley's equation that neglects the mean flow refraction effects. In the presence of a semi-infinite half plane, this Green's function is replaced with the tailored Green's function of Ffowcs-Williams and Hall [17]. The second Green's function is a high-frequency asymptotic solution to Lilley's equation obtained by Balsa [18] and Wundrow and Khavaran [19]. This Green's function is modified to account for a scattering half-plane via the tailored Green's function of Ffowcs-Williams and Hall [17]. The spectral predictions obtained by each Green's function are compared to empirically obtained spectral measurements to determine the accuracy and ability to capture the acoustic spectrum in the far-field. These comparisons are performed for a range of different jet operating conditions and observer angles. The present approach has the ability to capture the refraction effects of fine-scale mixing noise at high-frequencies analytically, which is an advantage compared to existing numerical approaches.

II. Methodology

Sections A and B follow Tam and Auriault's [8] approach for predicting fine-scale mixing noise in the form of Lilley's equation. Section A develops the governing equation for acoustic pressure with the appropriate source term. In section B, the prediction equation for spectral density is reduced to a volume integral. The reader is encouraged to review Tam and Auriault's [8] work for further explanation of the analysis in sections A and B. Sections C, D, and E outline each individual Green's function that is implemented to obtain predictions of the spectral density for static and installed jets.

We define the jet coordinate system with origin at the center of the nozzle exit and the x direction parallel to the centerline axis with $+x$ in the downstream direction. The transverse y and z directions are orthogonal to x, with y positive in the vertical direction. In cylindrical coordinates, r is the magnitude of a point in the y–z plane, and ϕ is the azimuthal angle defined as 0° on the y axis. The coordinate vector is defined as $\mathbf{x} = (x, y, z)$ and $\mathbf{x} = (x, r, \phi)$ in Cartesian and cylindrical coordinates, respectively.

A. Governing Equation

The Favre-averaged Navier-Stokes momentum equation is

$$\bar{\rho}\frac{D\tilde{u}_i}{Dt} = \frac{\partial}{\partial x_j}\left(-\bar{p}\delta_{ij} + \bar{\tau}_{ij} - \overline{\rho u_i' u_j'}\right), \tag{1}$$

where x and t are space and time, $\bar{p}$ is the mean pressure, $\tilde{u}$ is the Favre-averaged velocity, u' is the fluctuating velocity, $\bar{\rho}$ is the mean density, $\bar{\tau}_{ij}$ is the mean shear stress, and $\overline{\rho u_i' u_j'}$ is the Reynolds stress. The material derivative is defined as

$$\frac{D}{Dt} = \frac{\partial}{\partial t} + \tilde{u}_j \frac{\partial}{\partial x_j}. \tag{2}$$

Following the assumption of Lighthill [20], who demonstrated that dissipation of acoustic energy into heat by viscosity and heat conduction is a slow process, the effect of viscous terms on the acoustic disturbances will be neglected.

The Reynolds stresses are approximated by a Boussinesq [21] eddy viscosity model. Upon invoking the assumption that the terms multiplying the eddy viscosity do not contribute to the acoustic field, the Reynolds stresses can be represented by the noise source term of Tam and Auriault [8]. We now linearize the Favre-averaged velocity in Eqn. 1 to obtain a system of equations governing the acoustic perturbations. The linearized momentum equation is supplemented with the linearized equation of energy, to form a closed system of equations for the acoustic pressure perturbation

$$\bar{\rho}\Big[\frac{\partial u_i}{\partial t} + \bar{u}_j\frac{\partial u_i}{\partial x_j} + u_j\frac{\partial \bar{u}_i}{\partial x_j}\Big] + \frac{\partial p}{\partial x_i} = -\frac{\partial q_s}{\partial x_i}, \tag{3}$$

$$\frac{\partial p}{\partial t} + \bar{u}_j\frac{\partial p}{\partial x_j} + \gamma\bar{p}\frac{\partial u_j}{\partial x_j} = 0, \tag{4}$$

and,

$$q_s = \frac{2}{3}\bar{\rho}k_s'. \tag{5}$$

Equations 3 and 4 are the linearized Euler equations governing the acoustic pressure perturbations, $k_s = 1/2\langle \mathbf{u}' \cdot \mathbf{u}' \rangle$ is the kinetic energy of fine-scale turbulence, k_s' is the time dependent portion of the kinetic energy of fine-scale turbulence, q_s is the unsteady pressure exerted by the fine-scale turbulence, and γ is the ratio of specific heats. Following Lilley [15], we assume a locally parallel mean flow, which is valid for a slowly diverging jet flow. The mean flow is non-zero in the axial direction, and the derivative is non-zero only in the orthogonal r coordinate. Performing the divergence of Eqn. 3, we obtain

$$\frac{D}{Dt}\frac{\partial u_i}{\partial x_i} + \frac{\partial}{\partial x_i}\frac{1}{\bar{\rho}}\frac{\partial p}{\partial x_i} = -2\frac{\partial \bar{u}_j}{\partial x_i}\frac{\partial u_i}{\partial x_j} - \frac{\partial}{\partial x_i}\frac{1}{\bar{\rho}}\frac{\partial q_s}{\partial x_i}. \tag{6}$$

In Eqn. 6, we make use of the linearized energy equation (Eqn. 4) and obtain Phillip's equation,

$$\frac{D^2 p}{Dt^2} - \frac{\partial}{\partial x_i}\frac{\gamma\bar{p}}{\bar{\rho}}\frac{\partial p}{\partial x_i} = 2\gamma\bar{p}\frac{\partial \bar{u}_j}{\partial x_i}\frac{\partial u_i}{\partial x_j} + \frac{\partial}{\partial x_i}\frac{\gamma\bar{p}}{\bar{\rho}}\frac{\partial q_s}{\partial x_i}. \tag{7}$$

The material derivative is performed on Eqn. 7. By making use of the following relation,

$$\frac{D}{Dt}\frac{\partial}{\partial x_j} = \frac{\partial}{\partial x_j}\frac{D}{Dt} - \frac{\partial \bar{u}_k}{\partial x_j}\frac{\partial}{\partial x_k}, \tag{8}$$

and the Euler equation,

$$\frac{Du_i}{Dt} = -\frac{1}{\bar{\rho}}\frac{\partial p}{\partial x_j}\delta_{ij}. \tag{9}$$

We obtain Lilley's equation

$$\frac{D}{Dt}\left(\frac{D^2 p}{Dt^2} - \frac{\partial}{\partial x_i}\bar{c}^2\frac{\partial p}{\partial x_i}\right) + 2\frac{\partial \bar{u}_j}{\partial x_i}\frac{\partial}{\partial x_j}\bar{c}^2\frac{\partial p}{\partial x_i} = -2\bar{\rho}\bar{c}^2\frac{\partial \bar{u}_j}{\partial x_i}\frac{\partial \bar{u}_k}{\partial x_j}\frac{\partial u_i}{\partial x_k} + \frac{D}{Dt}\frac{\partial}{\partial x_i}\bar{c}^2\frac{\partial q_s}{\partial x_i}, \tag{10}$$

where $\gamma\bar{p}\bar{\rho}^{-1} = \bar{c}^2$ is the mean speed of sound squared. The first term on the right hand side of Eqn. 10 is zero for locally parallel mean flows. Equation 10 then takes the simplified form,

$$\frac{D}{Dt}\left(\frac{D^2 p}{Dt^2} - \frac{\partial}{\partial x_i}\bar{c}^2\frac{\partial p}{\partial x_i}\right) + 2\frac{\partial \bar{u}_j}{\partial x_i}\frac{\partial}{\partial x_j}\bar{c}^2\frac{\partial p}{\partial x_i} = \frac{D}{Dt}\frac{\partial}{\partial x_i}\bar{c}^2\frac{\partial q_s}{\partial x_i}. \tag{11}$$

Equation 11 is Lilley's equation with a source term representing fine-scale jet mixing noise. The solution to Eqn. 11 for p is obtained through the convolution of the Green's function with the source terms,

$$p(\mathbf{x}, t) = \int_{-\infty}^{\infty}\cdots\int_{-\infty}^{\infty} g(\mathbf{x}, t|\mathbf{x}_s, t_s)\Lambda(\mathbf{x}_s, t_s)d\mathbf{x}_s dt_s, \tag{12}$$

where Λ is,

$$\Lambda = \frac{D}{Dt}\frac{\partial}{\partial x_i}\left(\bar{c}^2\frac{\partial q_s}{\partial x_i}\right). \tag{13}$$

Equation 12 is the solution for the acoustic pressure. The spatial coordinate vector $\mathbf{x}$ is the observer location, $\mathbf{x}_s$ is the source location, t is the observer time, and t_s is the source time. The source field is bounded by the jet envelope, therefore the spatial integrals are zero outside of the jet, and for computational purposes these integrals can be performed over the volume of the jet.

We seek to rearrange Eqn. 12 such that we recover the pressure solution of Tam and Auriault [8] with a Green's function that is modified to account for the Laplacian operator of the source term. In Appendix A, it is shown for a locally parallel jet in the cylindrical coordinate system that Eqn. 12 can be rearranged to the following form,

$$p(\mathbf{x},t) = \int_{-\infty}^{\infty}\cdots\int_{-\infty}^{\infty}\frac{Dq_s}{Dt_s}\nabla_s\cdot\bar{c}_s^2\nabla_s g + \left[\frac{\partial g}{\partial x_s}\frac{1}{r_s}\frac{\partial}{\partial r_s}\left(r\bar{c}_s^2\frac{\partial \bar{u}_s}{\partial r_s}\right) - \frac{\partial}{\partial r_s}\left(\bar{c}_s^2\frac{\partial \bar{u}_s}{\partial r_s}\frac{\partial g}{\partial x_s}\right)\right] q_s d\mathbf{x}_s dt_s, \tag{14}$$

where the subscript "s" denotes evaluation of derivatives and other quantities at the source location. The second term in Eqn. 14 is a consequence of formulating the governing equation of acoustic pressure in terms of Lilley's equation. The first term contains the source term of Tam and Auriault [8] with a Laplacian operator acting on the Green's function of Lilley's equation. In the case of negligible mean flow refraction effects, the second term of Eqn. 14 may be neglected. We now represent the Green's function as its inverse Fourier transform,

$$g(\mathbf{x},t;\mathbf{x}_s,t_s) = \int_{-\infty}^{\infty} G(\mathbf{x},\mathbf{x}_s,\omega)e^{-i\omega(t-t_s)}d\omega, \tag{15}$$

and move $\nabla_s\cdot\bar{c}_s^2\nabla_s$ inside the integral. The resulting Green's function in the frequency domain is

$$\mathcal{G}(\mathbf{x},\mathbf{x}_s,\omega) = \nabla_s\cdot\bar{c}_s^2\nabla_s G(\mathbf{x},t;\mathbf{x}_s,\omega). \tag{16}$$

In a similar manner, the second term in Eqn. 14 can be represented in the frequency domain as,

$$\mathbb{G}(\mathbf{x},\mathbf{x}_s,\omega) = \left[\frac{\partial G}{\partial x_s}\frac{1}{r_s}\frac{\partial}{\partial r_s}\left(r\bar{c}_s^2\frac{\partial \bar{u}_s}{\partial r_s}\right) - \frac{\partial}{\partial r_s}\left(\bar{c}_s^2\frac{\partial \bar{u}_s}{\partial r_s}\frac{\partial G}{\partial x_s}\right)\right]. \tag{17}$$

The pressure solution is now represented by,

$$p(\mathbf{x},t) = \int_{-\infty}^{\infty}\cdots\int_{-\infty}^{\infty}\left[\mathcal{G}(\mathbf{x},\mathbf{x}_s,\omega)\Gamma(\mathbf{x}_s,t_s) + \mathbb{G}(\mathbf{x},\mathbf{x}_s,\omega)\Gamma_q(\mathbf{x}_s,t_s)\right]e^{-i\omega(t-t_s)}d\omega d\mathbf{x}_s dt_s, \tag{18}$$

where $\Gamma(\mathbf{x}_s,t_s) = Dq_s/Dt_s$ is the source term of Tam and Auriault [8] and $\Gamma_q(\mathbf{x}_s,t_s) = q_s$.

B. Spectral Density of the Acoustic Field

The spectral density of the acoustic field at the observer location is given by the Weiner-Khintchine theorem [22] as the Fourier transform of the autocorrelation. The spectral density function will be shown to simplify to the spectral density found by Tam and Auriault [8] with a different Green's function that represents the Laplacian of the Green's function solution to Lilley's equation (Eqn. 11). The spectral density is,

$$S(\mathbf{x},\omega) = \frac{1}{2\pi}\int_{-\infty}^{\infty}\langle p(\mathbf{x},t), p(\mathbf{x},t+\tau)\rangle e^{i\omega\tau}d\tau, \tag{19}$$

where ω is the acoustic angular frequency, $t+\tau$ is the delayed time, and $\langle\rangle$ is the ensemble average. The autocorrelation of pressure is the expectation of the pressure signal at $(\mathbf{x}_1,t_1,\omega_1)$ multiplied by the conjugate of the delayed pressure signal at $(\mathbf{x}_2,t_2,\omega_2)$. The autocorrelation of pressure is represented as,

$$\begin{aligned}\left\langle p(\mathbf{x},t), p(\mathbf{x},t+\tau)\right\rangle = \int_{-\infty}^{\infty}\cdots\int_{-\infty}^{\infty}\Big[&\mathcal{G}(\mathbf{x},\mathbf{x}_1,\omega_1)\mathcal{G}^*(\mathbf{x},\mathbf{x}_2,\omega_2)\left\langle\Gamma(\mathbf{x}_1,t_1),\Gamma(\mathbf{x}_2,t_2)\right\rangle \\ &+ \mathbb{G}(\mathbf{x},\mathbf{x}_1,\omega_1)\mathbb{G}^*(\mathbf{x},\mathbf{x}_2,\omega_2)\left\langle\Gamma_q(\mathbf{x}_1,t_1),\Gamma_q(\mathbf{x}_2,t_2)\right\rangle\Big]e^{-i\omega_1(t-t_1)+i\omega_2(t-t_2)+i\omega_2\tau}d\omega_1 d\omega_2 d\mathbf{x}_1 d\mathbf{x}_2 dt_1 dt_2,\end{aligned} \tag{20}$$

where subscripts 1 and 2 represent the integrated variables and * denotes conjugation. Taking the integral over τ, the spectral density can now be represented by,

$$S(\mathbf{x},\omega) = \int_{-\infty}^{\infty}\dots\int_{-\infty}^{\infty}\Big[\mathcal{G}(\mathbf{x},\mathbf{x}_1,\omega_1)\mathcal{G}^*(\mathbf{x},\mathbf{x}_2,\omega_2)\big\langle\Gamma(\mathbf{x}_1,t_1)\Gamma(\mathbf{x}_2,t_2)\big\rangle + \mathbb{G}(\mathbf{x},\mathbf{x}_1,\omega_1)\mathbb{G}^*(\mathbf{x},\mathbf{x}_2,\omega_2)\big\langle\Gamma_q(\mathbf{x}_1,t_1)\Gamma_q(\mathbf{x}_2,t_2)\big\rangle\Big]e^{-i(\omega_1-\omega_2)t+i\omega_1t_1-i\omega_2t_2}\delta(\omega+\omega_2)d\omega_1d\omega_2d\mathbf{x}_1d\mathbf{x}_2dt_1dt_2. \quad (21)$$

The space-time correlation function for the source term Γ is equal to Tam and Auriault's [8] correlation function. The resulting correlation function for Γ is

$$\big\langle\Gamma(\mathbf{x}_1,t_1),\Gamma(\mathbf{x}_2,t_2)\big\rangle = \frac{\hat{q}_s^2}{\tau_s^2}\exp\left[-\frac{|\xi|}{\bar{u}\tau_s}-\frac{ln(2)}{l_s^2}\left((\xi-\bar{u}\tau)^2+\eta^2+\zeta^2\right)\right], \quad (22)$$

Similarly, the correlation function for Γ_q is

$$\big\langle\Gamma_q(\mathbf{x}_1,t_1),\Gamma_q(\mathbf{x}_2,t_2)\big\rangle = \hat{q}_s^2\exp\left[-\frac{|\xi|}{\bar{u}\tau_s}-\frac{ln(2)}{l_s^2}\left((\xi-\bar{u}\tau)^2+\eta^2+\zeta^2\right)\right], \quad (23)$$

where $\hat{q}_s$ is the root mean square (rms) value of the pressure associated with fine-scale turbulence. The separation vector terms are $\xi = x_1 - x_2$, $\eta = y_1 - y_2$, $\zeta = z_1 - z_2$, and $\tau = t_1 - t_2$. The time scale of fine-scale turbulence is represented as τ_s, and the length scale of the fine-scale turbulence is represented by l_s. When combining Eqns. 22 and 23 with Eqn. 21, we obtain the following,

$$S(\mathbf{x},\omega) = \int_{-\infty}^{\infty}\dots\int_{-\infty}^{\infty}\left[\mathcal{G}(\mathbf{x},\mathbf{x}_1,\omega_1)\mathcal{G}^*(\mathbf{x},\mathbf{x}_2,\omega_2)\frac{\hat{q}_s^2}{\tau_s^2}+\mathbb{G}(\mathbf{x},\mathbf{x}_1,\omega_1)\mathbb{G}^*(\mathbf{x},\mathbf{x}_2,\omega_2)\hat{q}_s^2\right]$$
$$\times\exp\left[-\frac{|\xi|}{\bar{u}\tau_s}-\frac{ln(2)}{l_s^2}\left((\xi-\bar{u}\tau)^2+\eta^2+\zeta^2\right)\right]\exp\left[-i(\omega_1-\omega_2)t+i\omega_1t_1-i\omega_2t_2\right]\delta(\omega+\omega_2)d\omega_1d\omega_2d\mathbf{x}_1d\mathbf{x}_2dt_1dt_2. \quad (24)$$

It is now possible to reduce Eqn. 24 to a single volume integral over the source field. Following the steps of Tam and Auriault [8], we make the substitution $s = \tau - \xi\bar{u}^{-1}$ to compute the integral over t_1. The integral over t_1 is thus transformed into a Gaussian integral that can be evaluated analytically. The following integral over t_2 results in $2\pi\delta(\omega_1-\omega_2)$. The integrals over ω_1 and ω_2 are simply computed using the properties of the delta function. Thus, Eqn. 24 is simplified to an integral over $\mathbf{x}_1$ and $\mathbf{x}_2$,

$$S(\mathbf{x},\omega) = 2\pi\left(\frac{\pi}{ln(2)}\right)^{\frac{1}{2}}\int_{-\infty}^{\infty}\dots\int_{-\infty}^{\infty}\left[\mathcal{G}(\mathbf{x},\mathbf{x}_1,\omega_1)\mathcal{G}^*(\mathbf{x},\mathbf{x}_2,\omega_2)\frac{\hat{q}_s^2}{\tau_s^2}+\mathbb{G}(\mathbf{x},\mathbf{x}_1,\omega_1)\mathbb{G}^*(\mathbf{x},\mathbf{x}_2,\omega_2)\hat{q}_s^2\right]\frac{l_s}{\bar{u}}$$
$$\times\exp\left[-\frac{|\xi|}{\bar{u}\tau_s}-\frac{ln(2)}{l_s^2}\left(\eta^2+\zeta^2\right)\right]\exp\left[-i\frac{\xi}{\bar{u}}\omega-\frac{l_s^2}{4\bar{u}^2ln(2)}\omega^2\right]d\mathbf{x}_1d\mathbf{x}_2. \quad (25)$$

The Green's functions in the $\mathbf{x}_1$ coordinates can be related to the Green's functions of the $\mathbf{x}_2$ coordinates by a phase factor,

$$\mathcal{G}^*(\mathbf{x},\mathbf{x}_1,\omega) \simeq \mathcal{G}^*(\mathbf{x},\mathbf{x}_2,\omega)\exp\left[\frac{i\omega}{c_\infty\|\mathbf{x}\|}\mathbf{x}\cdot\boldsymbol{\eta}\right] \quad (26)$$

and

$$\mathbb{G}^*(\mathbf{x},\mathbf{x}_1,\omega) \simeq \mathbb{G}^*(\mathbf{x},\mathbf{x}_2,\omega)\exp\left[\frac{i\omega}{c_\infty\|\mathbf{x}\|}\mathbf{x}\cdot\boldsymbol{\eta}\right], \quad (27)$$

where $\boldsymbol{\eta}$ is the seperation vector between $\mathbf{x}_1$ and $\mathbf{x}_2$ coordinates. For a locally parallel mean flow, $\mathbf{x}\cdot\boldsymbol{\eta}$ can be approximated by $\mathbf{x}\cdot\boldsymbol{\eta} \simeq \|\mathbf{x}\|(x_1 - x_2)\cos\theta$, where θ is the angle between the downstream axis and the observer.

The integral over $\mathbf{x}_1$ of Eqn. 25 can now be evaluated. The integrals are evaluated by making the transformation $(\xi, \eta, \zeta) = (x_1 - x_2, y_1 - y_2, z_1 - z_2)$. The integrals over η and ζ are Gaussian integrals. The integral over ξ is then performed to obtain the following volume integral for spectral density,

$$S(\mathbf{x},\omega) = 4\pi\left(\frac{\pi}{ln(2)}\right)^{3/2}\int_{-\infty}^{\infty}\int_{-\infty}^{\infty}\int_{-\infty}^{\infty}\hat{q}_s^2 l_s^3\left[\frac{1}{\tau_s}|\mathcal{G}(\mathbf{x},\mathbf{x}_s,\omega)|^2 + \tau_s|\mathbb{G}(\mathbf{x},\mathbf{x}_s,\omega)|^2\right] \times \exp\left[-\omega^2\frac{l_s^2}{4\bar{u}^2 ln(2)}\right] \Bigg/ \left[1+\omega^2\tau_s^2\left(1-\frac{\bar{u}}{c_\infty}cos\theta\right)^2\right] d\mathbf{x}_s. \quad (28)$$

Equation 28 is the fine-scale prediction model developed by Tam and Auriault [8] with a modified Green's function and an additional term, $\tau_s|\mathbb{G}|^2$. The Green's functions in Eqn. 28 are the Green's function for Lilley's equation subject to the operations in Eqns. 16 and 17 for $\mathcal{G}$ and $\mathbb{G}$, respectively. The flow variables such as $\bar{u}$ and $\bar{c}$ are determined from RANS simulations. The length scale, time scale, and fine-scale turbulent pressure are semi-empirically determined from steady RANS simulations. The time scale of the fine-scale turbulence τ_s, determined from a $k-\omega$ turbulence model is found to be much smaller than unity ($\tau_s \ll 1$) for the jet cases considered in this paper. When comparing $\tau_s^{-1}|\mathcal{G}|^2$ and $\tau_s|\mathbb{G}|^2$, it is found that the latter term can be considered negligible, indicating that q_s is small compared to Dq/Dt_s. Thus, Eqn. 28 can be reduced to,

$$S(\mathbf{x},\omega) = 4\pi\left(\frac{\pi}{ln(2)}\right)^{3/2}\int_{-\infty}^{\infty}\int_{-\infty}^{\infty}\int_{-\infty}^{\infty}\frac{\hat{q}_s^2 l_s^3}{\tau_s}|\mathcal{G}(\mathbf{x},\mathbf{x}_s,\omega)|^2 \times \exp\left[-\omega^2\frac{l_s^2}{4\bar{u}^2 ln(2)}\right] \Bigg/ \left[1+\omega^2\tau_s^2\left(1-\frac{\bar{u}}{c_\infty}cos\theta\right)^2\right] d\mathbf{x}_s. \quad (29)$$

The fine-scale turbulent length and time scales are adopted from Tam and Auriault [8] who used a modified $k-\epsilon$ turbulence model developed by Thies and Tam [23]. The present work uses the Mentor [24] Shear Stress Transport (SST) $k-\omega$ turbulence model in the RANS calculation. The specific dissipation rate ω_t is related to ϵ by $\omega_t = \epsilon/0.09k$. Therefore, the length and time scales for the fine-scale turbulence are represented as

$$l_s = c_l\frac{1}{0.09}\frac{k^{\frac{1}{2}}}{\omega_t} \quad (30)$$

and

$$\tau_s = \frac{1}{0.09}\frac{c_\tau}{\omega_t}. \quad (31)$$

The term $\hat{q}_s$ is

$$\hat{q}_s = c_q q, \quad (32)$$

where c_q, c_τ, and c_l are empirically determined constants.

C. The Free-Space Green's Function

A Green's function is developed that neglects mean flow refraction effects (i.e. the environment is quiescent). This Green's function is used to obtain a first approximation of the acoustic spectrum. In the sideline direction ($\theta = 90°$) refraction effects are small. When the incident wave across a region with a velocity gradient has an angle of incidence of 90° the angle of the transmitted wave will not be altered [25]. Thus, a free space Green's function that neglects refraction effects from a velocity gradient will compare favorably with measurement in the sideline direction. Using Eqn. 11, we set $\partial_j\bar{u}_i = 0$ and represent the source term by delta functions,

$$\frac{\partial}{\partial t}\left(\frac{\partial^2 g_0}{\partial t^2} - c_\infty^2\frac{\partial^2 g_0}{\partial x_i \partial x_i}\right) = \delta(\mathbf{x}-\mathbf{x}_s)\delta(t-t_s). \quad (33)$$

Upon taking the Fourier transform of Eqn. 33, we obtain

$$\frac{\omega^2}{c_\infty^2}\hat{g}_0 + \frac{\partial^2 \hat{g}_0}{\partial x_i \partial x_i} = \frac{-i}{2\pi\omega c_\infty^2}\delta(\mathbf{x}-\mathbf{x}_s)e^{i\omega t_s}, \tag{34}$$

where $\hat{g}_0$ is,

$$\hat{g}_0 = \frac{1}{2\pi}\int_{-\infty}^{\infty} g_0 e^{i\omega t}\, dt. \tag{35}$$

Equation 34 is the Helmholtz equation, the Green's function solution is

$$\hat{g}_0(\mathbf{x},\omega,\mathbf{x}_s,t_s) = \frac{i}{8\pi^2\omega c_\infty^2}\frac{\exp\left(i\frac{\omega}{c_\infty}|\mathbf{x}-\mathbf{x}_s|\right)}{|\mathbf{x}-\mathbf{x}_s|}e^{i\omega t_s}. \tag{36}$$

The temporal Green's function can be represented by its inverse Fourier transform as

$$g_0(\mathbf{x},t;\mathbf{x}_s,t_s) = \int_{-\infty}^{\infty}\hat{g}_0(\mathbf{x},\mathbf{x}_s,\omega)e^{-i\omega t}\,d\omega = \int_{-\infty}^{\infty} G_0(\mathbf{x},\mathbf{x}_s,\omega)e^{-i\omega(t-t_s)}d\omega \tag{37}$$

where

$$G_0(\mathbf{x},\mathbf{x}_s,\omega) = \frac{i}{8\pi^2\omega c_\infty^2}\frac{\exp\left(i\frac{\omega}{c_\infty}|\mathbf{x}-\mathbf{x}_s|\right)}{|\mathbf{x}-\mathbf{x}_s|} = \frac{i}{2\pi\omega c_\infty^2}G_f. \tag{38}$$

G_f is defined as,

$$G_f(\mathbf{x},\mathbf{x}_s,\omega) = \frac{\exp\left(i\frac{\omega}{c_\infty}|\mathbf{x}-\mathbf{x}_s|\right)}{4\pi|\mathbf{x}-\mathbf{x}_s|}. \tag{39}$$

This free-space Green's function is used to predict the spectral density of acoustic pressure without the effect of refraction. For $\partial_j \bar{u}_i = 0$, we have $\mathbb{G} = 0$, and $\mathcal{G}$ is evaluated with Eqn. 38 to obtain

$$\begin{aligned}\mathcal{G}_0(\mathbf{x},\mathbf{x}_s,\omega) &= \left(\frac{\partial \bar{c}_s^2}{\partial r_s}\frac{\partial}{\partial r_s} + \bar{c}_s^2\nabla_s^2\right)\left[\frac{i}{8\pi^2\omega c_\infty^2}\frac{\exp\left(i\frac{\omega}{c_\infty}|\mathbf{x}-\mathbf{x}_s|\right)}{|\mathbf{x}-\mathbf{x}_s|}\right] \\ &= \frac{-i\omega\bar{c}_s^2}{8\pi^2 c_\infty^4}\frac{\exp\left(i\frac{\omega}{c_\infty}|\mathbf{x}-\mathbf{x}_s|\right)}{|\mathbf{x}-\mathbf{x}_s|} + \frac{i}{8\pi^2\omega c_\infty}\frac{\partial \bar{c}_s^2}{\partial r_s}\frac{r_s - r\cos(\phi-\phi_s)}{|\mathbf{x}-\mathbf{x}_s|^2}\left(\frac{i\omega}{c_\infty} - \frac{1}{|\mathbf{x}-\mathbf{x}_s|}\right)\exp\left(i\frac{\omega}{c_\infty}|\mathbf{x}-\mathbf{x}_s|\right).\end{aligned} \tag{40}$$

The free-space Green's function is obtained using the assumption of $\partial_j \bar{u}_i = 0$ and $\bar{c} = c_\infty$. Therefore, the spatial derivative of $\bar{c}_s^2$ is zero and $\mathcal{G}_0$ is represented as,

$$\mathcal{G}_0(\mathbf{x},\mathbf{x}_s,\omega) = \frac{-i\omega}{2\pi c_\infty^2}G_f. \tag{41}$$

D. Green's Function with Refraction Effects

The modified Green's function in Eqn. 29 ($\mathcal{G}$) will account for refraction effects of the jet shear layer if G is the exact Green's function solution of Eqn. 11. The Green's function solution of Eqn. 11 has not yet been obtained without the use of numerical methods. In this section, we shall examine a high-frequency asymptotic Green's function solution to Lilley's equation that has been obtained by Balsa [18] as well as Wundrow and Khavaran [19]. The benefit of implementing the asymptotic solution of Wundrow and Khavaran [19] is that the derivatives in $\mathcal{G}$ can be performed analytically. In using the high-frequency asymptotic Green's function solution of Lilley's equation, we assume that refraction effects are minimal on acoustic waves with wavelength λ much larger than the shear layer thickness δ_s (i.e. $\lambda \gg \delta_s$). The viability of this assumption will be examined in the results section when Eqn. 28 is compared to the measurements of Brown and Bridges [16].

Balsa [18] considered the case where the acoustic source is located sufficiently close to the jet axis, such that the azimuthal mode number is of order one $n \sim O(1)$. Wundrow and Khavaran [19] consider Balsa's [18] scaling to be the "quasi-symmetric" solution, and present their own form of the solution. Wundrow and Khavaran [19] also consider the case in which the distance between the source and jet axis is sufficiently large and refer to this as the asymmetric approximation. We will consider here the quasi-symmetric solution, for more details the reader is referred to Wundrow and Khavaran [19] or Balsa [18]. The quasi-symmetric solution G_q is,

$$G_q\left(\boldsymbol{x}, \boldsymbol{x}_s, \omega\right) \sim \frac{-i}{\overline{c}_s c_\infty \omega} \frac{1}{\left(1 - M_s cos\theta\right)^2} G_f \mathcal{R}_\omega, \tag{42}$$

where R_ω is solved using a WKB approach, and is discussed in Wundrow and Khavaran [19]. The resulting form of R_ω is,

$$R_\omega \sim \exp\left[i \frac{\omega}{c_\infty}\left(\chi - R\sin^2\left(\theta\right) - \chi_s \cos\left(\phi - \phi_s\right)\right)\right], \tag{43}$$

where R is the distance from source to observer, θ is the observer angle, and ϕ is the azimuthal angle for the observer or source (ϕ_s), respectively. The variable χ is defined as,

$$\chi(r) = \int_0^r Q(r')dr'. \tag{44}$$

For small r, χ is approximately equal to rQ. The function Q is defined by,

$$Q = \sqrt{\Phi^2 - \cos^2(\theta)}. \tag{45}$$

Then, Φ is a function of the mean flow variables defined by,

$$\Phi(r) = \frac{c_\infty - \overline{u}\cos(\theta)}{\overline{c}}. \tag{46}$$

The modified Green's function $\mathcal{G}_q$ can then be determined by performing derivatives of the Laplacian type operator acting on G_q,

$$\mathcal{G}_q = \nabla_s \cdot \overline{c}_s^2 \nabla_s G_q. \tag{47}$$

The quasi-symmetric Green's function G_q is derived with the assumption that the source is close to the centerline, thus it is expected that terms in G_q that scale as r_s^{-1} or r_s^{-2} will be dominant. As a result of the near-axis source scaling in the derivation of G_q it is assumed that the acoustic field will become increasingly axisymmetric. Thus, azimuthal derivatives of G_q are neglected. With this source scaling in mind the Green's function is simplified to,

$$\mathcal{G}_q = \overline{c}_s^2 \frac{1}{r_s} \frac{\partial G_q}{\partial r_s}. \tag{48}$$

When the derivative operation is performed on G_q and terms of order $O\left(R^{-2}\right)$ or less are neglected, the expression for $\mathcal{G}_q$ becomes

$$\mathcal{G}_q = \frac{\overline{c}_s^2}{r_s}\left[-\frac{\overline{c}_s'}{\overline{c}_s} + \frac{2M_s' \cos\theta}{1 - M_s\cos\theta} - \frac{ik_0}{4\pi}\frac{r\cos(\phi - \phi_s)}{R} + ik_0\left(\cos(\phi - \phi_s)\frac{r^3}{R^3} - 2\frac{r}{R} - Q_s\cos(\phi - \phi_s)\right)\right] G_q, \tag{49}$$

where $'$ denotes differentiation with respect to r_s.

E. Green's Function with Shielding Effects

When a semi-infinite flat plate is present in the jet acoustic field, acoustic waves will scatter due to their interaction with the solid surface. Ffowcs-Williams and Hall [17] demonstrated how this scattering affect can be accounted for by using a Green's function solution to the Helmholtz equation that is tailored to satisfy the boundary conditions on the plate. To obtain spectral predictions of the radiated sound in the presence of this surface, it was assumed that the surface does not alter the jet flow, and that the surface does not contain acoustic sources. The equation governing the motion of

the acoustic waves in the far-field is the Helmholtz equation. Thus, we propose to replace the G_f in Eqns. 41 and 42 with the tailored Green's function solution given in Ffowcs-Williams and Hall [17]. This is similar to the approach of Smith and Miller [10]. The tailored Green's function of Ffowcs-Williams and Hall [17] is,

$$G_t\left(\boldsymbol{x};\boldsymbol{x}_s,x_p,y_p,\omega\right)=\frac{e^{(1/4)\kappa\pi}}{\sqrt{\pi}}\left(\frac{e^{-i\kappa R}}{4\pi R}\int_{-\infty}^{u_R}e^{-iu^2}du+\frac{e^{-i\kappa R'}}{4\pi R'}\int_{-\infty}^{u_{R'}}e^{-iu^2}du\right), \tag{50}$$

where $u_\square$ is

$$u_\square=2\sqrt{\frac{\kappa\varrho\varrho_s}{B+\square}}\cos\left(\frac{\beta\mp\beta_s}{2}\right) \tag{51}$$

and $\square$ is a placeholder for R or R' and the sign in the cosine term is negative for R and positive for R'.

Here, R and R' are the distances between the observer and the source, as well as the observer and image source, respectively. The image source is defined as the mirror image of the source across the plane of the impingement plate. The coordinate system (ϱ,β,z) originates on the trailing edge of the plate with the z-axis parallel to the edge and $\beta=0$ on the flat plate. We define ϱ, β, and z for an observer or source $\mathbf{A}=(a_1,a_2,a_3)$ as

$$\varrho=\sqrt{(a_2-y_p)^2+(a_1-x_p)^2}, \tag{52}$$

$$\beta=\pi-cos^{-1}\left(\frac{x_p(a_1-x_p)+y_p(a_2-y_p)}{\sqrt{(a_2-y_p)^2+(a_1-x_p)^2}\sqrt{(y_p)^2+(x_p)^2}}\right), \tag{53}$$

and

$$z=a_3. \tag{54}$$

The variable κ is the wavenumber defined as ωc_∞^{-1} and B is

$$B=\sqrt{(\varrho+\varrho_s)^2+(z-z_s)^2}. \tag{55}$$

We substitute $u=\sqrt{\frac{\pi}{2}}t$ and make use of the symmetric relations of Fresnel integrals (see Zhang et al. [26] for details). We obtain expressions for both integrals which are

$$\int_{-\infty}^{u_\square}e^{-iu^2}du=\frac{1}{2}\sqrt{\frac{\pi}{2}}\left[2C\left(\sqrt{\frac{2}{\pi}}u_\square\right)+1\right]-i\frac{1}{2}\sqrt{\frac{\pi}{2}}\left[2S\left(\sqrt{\frac{2}{\pi}}u_\square\right)+1\right] \tag{56}$$

where $C(x)$ and $S(x)$ represent the Fresnel cosine and sine integrals with upper bound x, respectively.

III. Results

A. RANS Validation

The commercial CFD software package Star-CCM+ [27] is used to perform Steady-RANS simulations of a small metal chevron SMC000 convergent nozzle operating at NPR = 1.861 and TTR = 1.00. The RANS simulations are validated with the particle image velocimetry (PIV) data of Bridges and Wernet [28]. Comparisons are made with centerline velocity measurements and radial profile measurements of the axial velocity, $\bar{u}$, and turbulent kinetic energy (TKE).

The RANS simulation performed is a finite volume second order implicit integration. The geometry of the domain includes the contour of the SMC000 nozzle with the outgoing boundary condition $50D$ downstream and the height of the domain $25D$ from the centerline. A stagnation inlet boundary condition is imposed in the nozzle, and the free-stream boundary condition is set to $M_\infty=0.1$ to sustain numerical stability of the solver. The centerline is set as an axis of symmetry. The number of elements in the domain is 110,778. The smallest elements within the domain are on the order of $0.03D$. Convergence is achieved for all setpoints after approximately 10,000 iterations. A grid independence study is performed to ensure stability of the simulation.

Figure 1 shows a comparison of the centerline velocity measurements of Bridges and Wernet [28] with the steady RANS results for the same nozzle at identical operating conditions. The steady RANS result shows an over-prediction of the core length by approximately 4 to 5 jet diameters. It was shown by Georgiadis et al. [29] that the Mentor-SST model over-predicts the core length by approximately 3 nozzle diameters at $M_j = 0.513$. Past the core length of the jet, the slope of decreasing jet velocity has the same slope as the measurement, which is approximately x^{-1}.

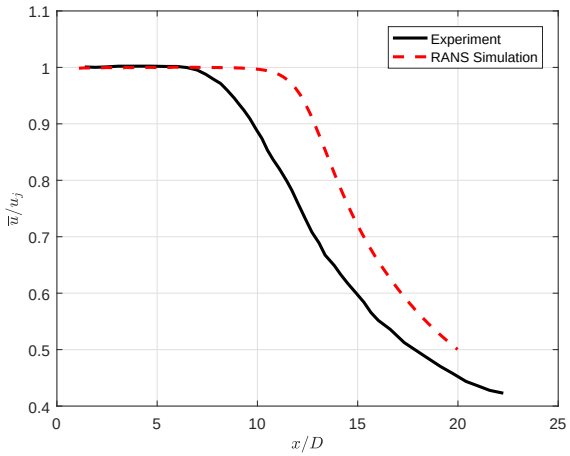

Fig. 1 Centerline profile of $\overline{u}u_j^{-1}$ at $rD^{-1} = 0$. Comparison of the steady RANS simulation results with the experimental results of Bridges and Wernet [28]. The SMC000 convergent nozzle operates at $M_j = 0.985$, NPR = 1.861, and TTR = 1.00.

Figure 2 shows radial profiles from the jet centerline to $rD^{-1} = 1$ at $xD^{-1} = 4$ for normalized axial velocity and TKE. Figure 2a shows good agreement with the experimental measurement of Bridges and Wernet [28]. At $rD^{-1} = 0.8$, the velocity of the RANS simulation begins to deviate from experimental measurement, which is due to the presence of an ambient Mach number of $M_\infty = 0.1$. This M_∞ is prescribed as the free-stream of the simulation to obtain numerical stability. Figure 2b shows an over-prediction of the TKE by the RANS simulation in the range of $0.45 < rD^{-1} < 0.7$ by approximately $ku_j^{-2} = 0.005$ at the location of maximum difference.

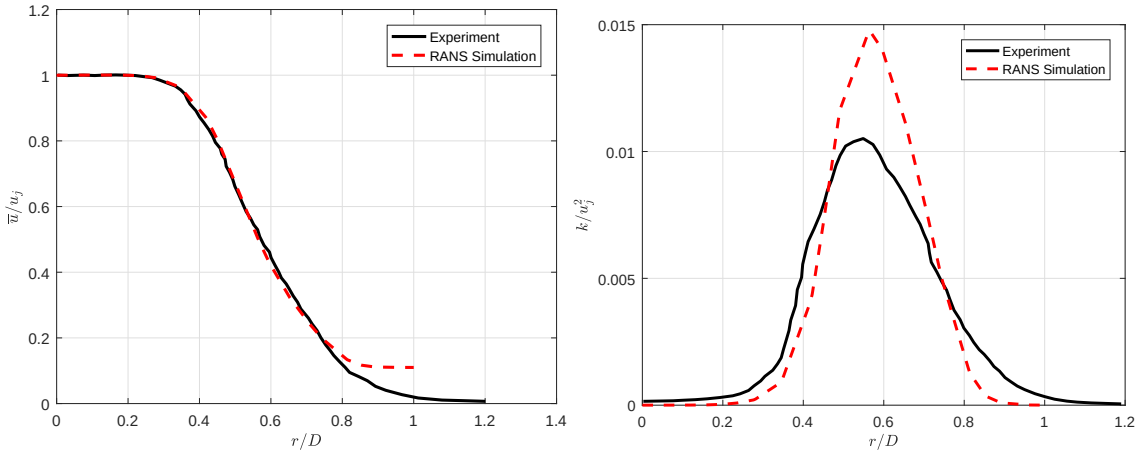

(a) $\overline{u}u_j^{-1}$ **(b) ku_j^{-2}**

Fig. 2 Radial profiles of $\overline{u}u_j^{-1}$ and ku_j^{-2} at $xD^{-1} = 4$. Comparison of the steady RANS simulation results with the experimental results of Bridges and Wernet [28]. The SMC000 convergent nozzle operates at $M_j = 0.985$, NPR = 1.861, and TTR = 1.00.

B. Mach Number Scaling

We now consider a static jet case with free-stream Mach number of zero and no scattering surfaces. The spectral density (Eqn. 29) with $\mathcal{G}_0$ and $\mathcal{G}_q$ is compared to the experimentally obtained acoustic spectra of Brown and Bridges [16]. Experimental setpoints 3, 5, and 7 are considered here. The results are plotted in terms of sound pressure level (SPL) per unit Strouhal number.

The coefficients c_q, c_τ, and c_l are calibrated for an observer angle of $\theta = 90°$ with $M_j = 0.985$ and TTR = 1.00. The source field is obtained using RANS simulations for an SMC000 convergent nozzle at $M_j = 0.513$, $M_j = 0.725$, and $M_j = 0.985$. These Mach numbers correspond to setpoints 3, 5, and 7 of the experimental database. The RANS results are used as input to Eqn. 29 for sideline predictions. The coefficients c_q, c_τ, and c_l are adjusted to match the spectrum at setpoint 7. Table 1 provides the Mach number, TTR, and NPR for each experimental setpoint considered.

Table 1 Experimental Setpoints of Brown and Bridges [16].

Setpoint	M_j	TTR	NPR
3	0.513	1.00	1.197
5	0.725	1.00	1.418
7	0.985	1.00	1.861

Figure 3 shows the scaling of Eqn. 29 with respect to Mach number of three cold subsonic jets. Both $\mathcal{G}_0$ and $\mathcal{G}_q$ are calibrated to fit the experimental noise spectrum at setpoint 7 for $\theta = 90°$. Once the calibration coefficients are found, the predictions using both $\mathcal{G}_0$ and $\mathcal{G}_q$ are calculated and compared to the data of Brown and Bridges [16] at each setpoint for $\theta = 90°$ and 120°. The free-space Green's function ($\mathcal{G}_0$) scales well with Mach number and observer angle. However, at higher frequencies the slope of the spectral predictions do not match the experimental data. This is most likely due to the inability of $\mathcal{G}_0$ to capture shear layer refraction effects. The high frequency asymptotic Green's function $\mathcal{G}_q$ shows better agreement of the spectral slope at high frequencies, with the slope of the spectrum matching the measurement at all setpoints. The magnitude of the $\mathcal{G}_q$ prediction matches the measurement in every case except for a slight under-prediction at $M_j = 0.985$ and $\theta = 90°$. For setpoint 7, at $\theta = 90°$ and 120°, there is an overlap between the prediction using $\mathcal{G}_q$ and the experimental data at high frequencies. This indicates that refraction effects for the high frequency radiated acoustic waves are captured by $\mathcal{G}_q$. At low frequencies, $\mathcal{G}_q$ is not expected to show any agreement with experimental data, due to the high frequency assumption that is used to obtain $\mathcal{G}_q$.

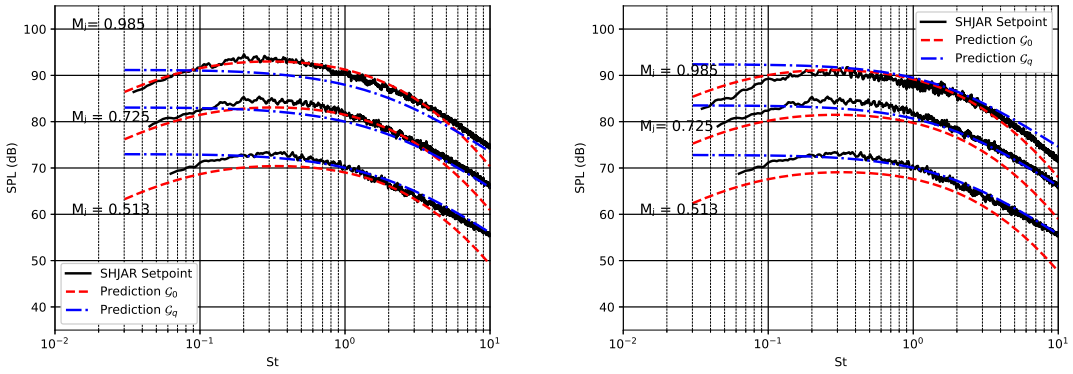

(a) $\theta = 90°$ **(b)** $\theta = 120°$

Fig. 3 Comparison of SPL at $R = 100D$ and $\phi = 0°$, for a) $\theta = 90°$ and b) 120°. Setpoints 3, 5, and 7 are considered, corresponding to $M_j = 0.513$, $M_j = 0.725$, and $M_j = 0.985$, respectively. Experimental measurements are from Brown and Bridges [16].

The Mach number scaling analysis provides a basis for calibrating the turbulence coefficients. Table 2 provides the turbulence coefficients determined by a best fit of the prediction to experimental data at $M_j = 0.513$ and $\theta = 90°$, along with the scaling coefficient c_g of the high frequency asymptotic Green's function $\mathcal{G}_q$.

Table 2 Calibration Coefficients for Eqn. 29.

$\mathcal{G}$	c_q	c_τ	c_l	c_g
$\mathcal{G}_0$	0.0036	0.255	0.085	NA
$\mathcal{G}_q$	0.0036	0.008	0.0015	2.03×10^{-4}

C. Freejet Predictions

The effect of the mean shear of the jet flow on the radiated acoustic waves is now investigated. Comparisons are made at several observer angles to assess the ability of $\mathcal{G}_q$ to capture refraction effects. The range of observer angles varies from 90° to 120° relative to the downstream axis in increments of 10°. This range is determined based on the availability of experimental measurements made by Brown and Bridges [16] and the accuracy of the quasi-symmetric Green's function, which even at high St numbers can under-predict the magnitude of the Green's function at downstream angles (see Wundrow and Khavaran [19] for details).

Figure 4 displays comparisons of the spectral density prediction for setpoint 7 at four different observer angles relative to experimental data. Both $\mathcal{G}_0$ and $\mathcal{G}_q$ compare well with the experimental data at all angles, with $\mathcal{G}_q$ showing a slightly better prediction at large Strouhal numbers. For $\theta \geq 110°$ $\mathcal{G}_q$ over-predicts the SPL at high Strouhal numbers by approximately $1-3$ dB. This is an improvement compared to the under prediction of $\mathcal{G}_0$ by about $2-5$ dB.

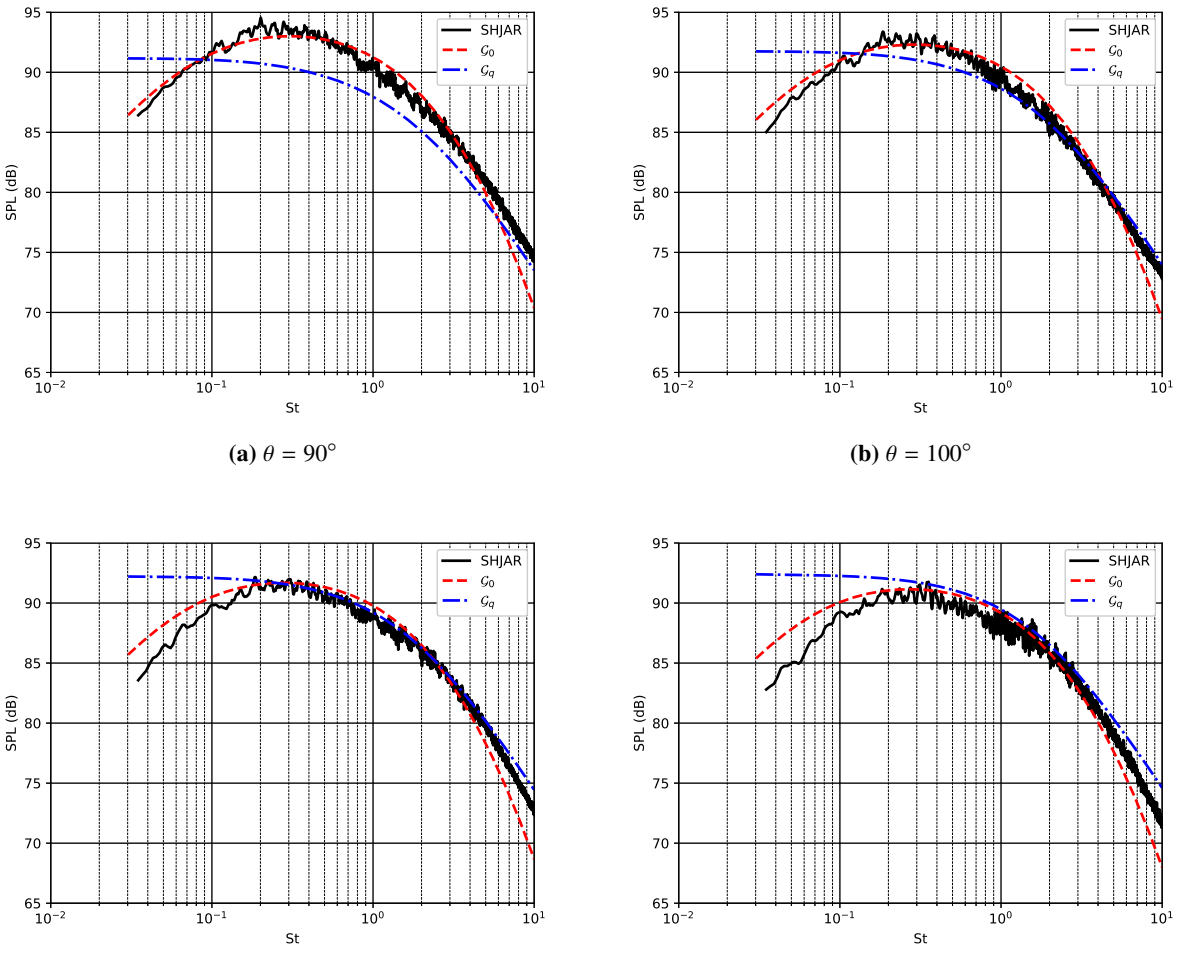

(a) $\theta = 90°$ **(b)** $\theta = 100°$

(c) $\theta = 110°$ **(d)** $\theta = 120°$

Fig. 4 Comparison of SPL at $R = 100D$, $90° \leq \theta \leq 120°$, and $\phi = 0°$. SMC000 convergent nozzle operating at $M = 0.985$, NPR = 1.861, and TTR = 1.00. Experimental measurements obtained from Brown and Bridges [16].

D. Prediction of Scattered Fine-Scale Mixing Noise

Attention is now turned to the situation in which the far-field acoustic waves are scattered by the presence of a solid plate. The Green's functions $\mathcal{G}_0$ and $\mathcal{G}_q$ remain valid as there exist no source terms on the plate. The free-space Green's function G_f is replaced by Eqn. 50, which includes the effects of the plate in the acoustic field. Predictions are compared to the experimental results of Brown [3]. The experimental setup of Brown [3] consists of a plate at some r/D distance below an axisymmetric jet ($1 \leq r/D \leq 16$), where the trailing edge of the plate varies between $2 \leq x/D \leq 20$.

Figure 5 presents spectral predictions of fine-scale mixing noise for a jet operating at setpoint 7 with and without the presence of a shielding plate at $xD^{-1} = 15$ and $rD^{-1} = 16$ for two observer angles on the shielded side of the plate. Results indicate that a more accurate prediction is made at high frequencies by $\mathcal{G}_q$ for large observer angles. For observer angles in the sideline direction and further downstream, $\mathcal{G}_0$ obtains better predictions. At $\theta = 120°$ the difference in decibels (ΔdB) at high frequencies is nearly indiscernible between $\mathcal{G}_q$ and the experiment, while there is approximately $\Delta dB = -10$ for $\mathcal{G}_0$. For observer angles of $\theta = 90°$ and farther downstream, $\mathcal{G}_q$ does not seem to have significant variation from the unshielded prediction, and over-predicts the spectrum at high frequencies. The solution of the Helmholtz equation in the presence of a semi-infinite flat plate ($\mathcal{G}_0$ in combination with Eqn. 50) gives better ΔdB predictions at these angles. In this instance, solutions to Lilley's equation in the presence of a semi-infinite flat plate are needed to more accurately capture both refraction and scattering effects. The assumption that the free-space Green's function term G_f in the quasi-symmetric Green's function of Wundrow and Khavaran [19] can be replaced by the tailored Green's function solution to the Helmholtz equation no longer appears to produce accurate results at $\theta \leq 90°$.

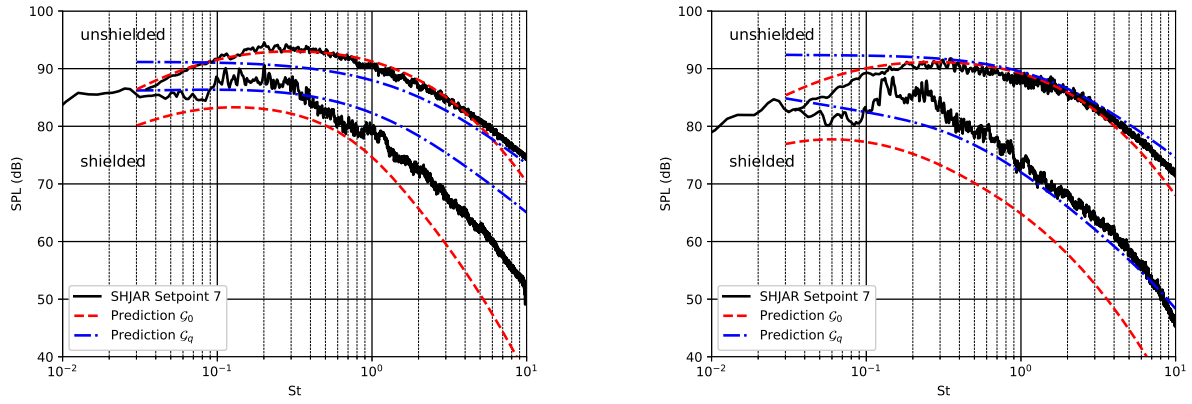

(a) $\theta = 90°$ **(b)** $\theta = 120°$

Fig. 5 Comparison of SPL on the shielded side of a flat plate ($xD^{-1} = 15$ and $rD^{-1} = 16$) at $R = 100D$, $\theta = 90°$ and $120°$, and $\phi = 0°$ from the nozzle center. The jet is issuing from a SMC000 convergent nozzle operating at $M = 0.985$, NPR = 1.861, and TTR = 1.00. Experimental measurements obtained from Brown [3].

Figure 6 compares SPL predictions at four different Strouhal numbers as a function of observer angle for a jet operating at setpoint 7 in the presence of a semi-infinite flat plate at $xD^{-1} = 15$ and $rD^{-1} = 16$. For observer angles $100° \leq \theta \leq 130°$ $\mathcal{G}_q$ shows an improved ΔdB prediction compared to the results using $\mathcal{G}_0$. At observer angles $\theta \leq 90°$, $\mathcal{G}_0$ shows a better ΔdB prediction at each frequency. $\mathcal{G}_0$ also appears to predict a slope of SPL as a function of θ that shows a better agreement with experimental data. This could be due to the formulation of the shielding Green's functions. When G_f is replaced with Eqn. 50 in $\mathcal{G}_0$, G_f still represents an exact solution to the Lilley equation when refraction effects are neglected and a flat-plate is present in the far-field. However, $\mathcal{G}_q$ was derived assuming that the integral in Wundrow and Khavaran [19] can be performed with the method of stationary phase. In their work, it was assumed that the Green's function would adhere to the Sommerfeld radiation as R approached infinity. When a plate is present in the far-field, the Green's function may not be able to be replaced by the Sommerfeld condition in the integral. A more exact solution for Lilley's equation when a semi-infinite flat plate is in the far-field will be required for more accuracy.

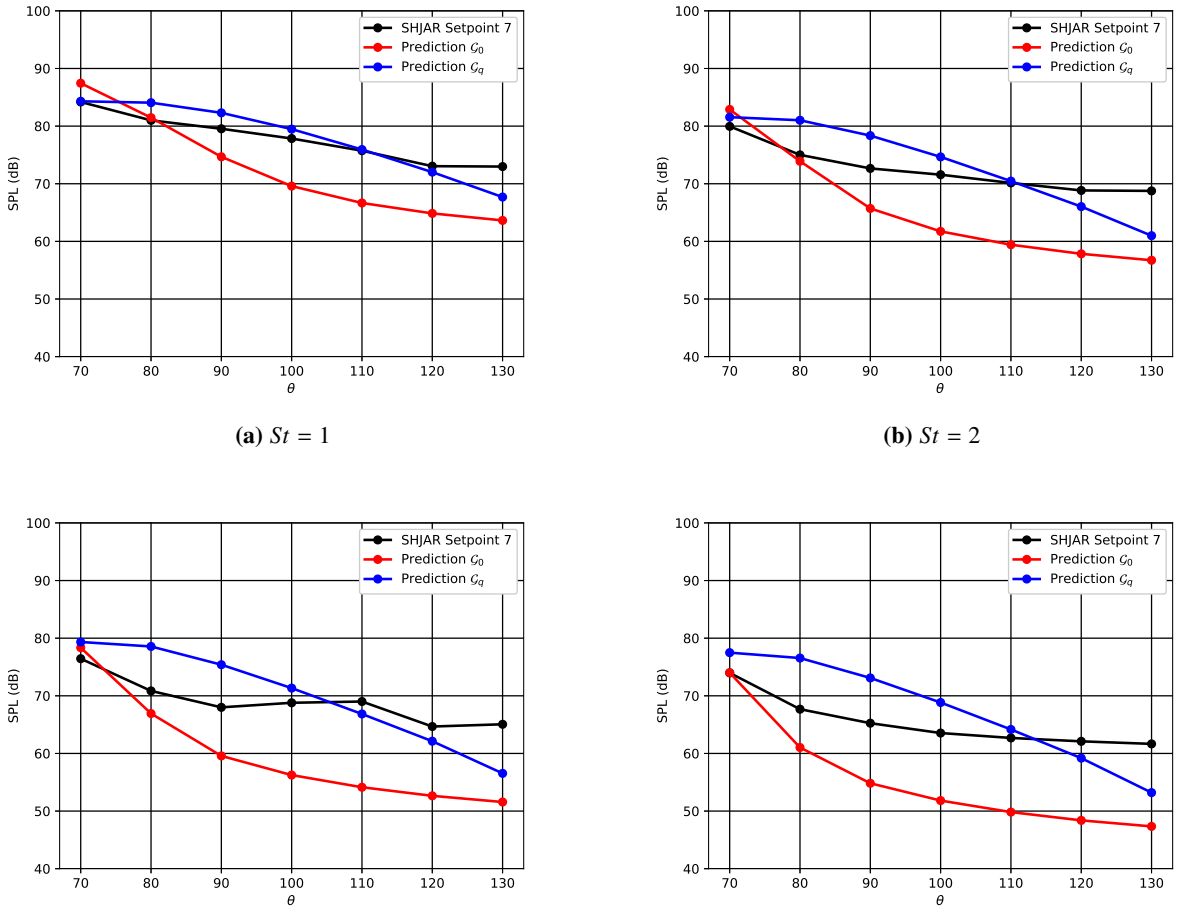

(a) $St = 1$ **(b)** $St = 2$

(c) $St = 3$ **(d)** $St = 4$

Fig. 6 Comparison of SPL on the shielded side of a flat plate ($xD^{-1} = 15$ **and** $rD^{-1} = 16$) **at** $R = 100D$ **and** $\phi = 0°$ **from the nozzle center. Predictions are computed at several different observer angles** $70° \leq \theta \leq 130°$ **from the downstream axis for 4 different Strouhal numbers. The jet is issuing from a SMC000 convergent nozzle operating at** $M = 0.985$**, NPR = 1.861, and TTR = 1.00. Experimental measurements obtained from Brown [3].**

IV. Summary and Conclusion

A. Lilley's Acoustic Analogy Formulation

Tam and Auriault's [8] prediction model for fine-scale mixing noise is modified by re-formulating the governing equations in terms of Lilley's equation. The Green's function is modified to account for the operator $\nabla \cdot \bar{c}^2 \nabla$ in the source term through the application of the divergence theorem, integration by parts, and Green's identities. The resulting spectral density formulation, Eqn. 29, is different from Tam and Auriault's [8] by a modified Green's function $\mathcal{G} = \nabla_s \cdot \bar{c}_s^2 \nabla_s G$ that accounts for refraction effects by the shear layer instead of the vector Green's function of the linearized Euler equations. The Green's function solution of Lilley's equation, $G(\mathbf{x}, \mathbf{x}_1, \omega)$, for the case of negligible shear layer refraction effects is the solution to the Helmholtz equation with a Dirac delta function source (Eqn. 34). Equation 29 is used in conjunction with Eqn. 41 to obtain a first approximation of the acoustic spectrum for a $M_j = 0.985$ jet operating at TTR = 1.00. Equation 29 is also compared to experimental measurements made in the sideline direction for three different jets operating at $0.513 \leq M_j \leq 0.985$ and TTR = 1.00 to assess the scalability of the predictions with jet Mach number. Results show a favorable comparison with measurements made by Brown and Bridges [16]. The comparisons with measurements shown in Figs. 3 and 4 provide a validation that Lilley's acoustic analogy can accurately capture the noise from fine-scale turbulence when the source model (Eqn. 5) of Tam and Auriault [8] is used.

Steady RANS simulation results for a jet produced by an SMC000 converging nozzle operating at $M_j = 0.985$ and TTR = 1.00 is obtained using the commercial CFD program Star-CCM+. Numerical results for the centerline velocity, TKE at $xD^{-1} = 4$, and velocity at $xD^{-1} = 4$, are compared with experimental measurements of Bridges and Wernet [28] to ensure the CFD results are accurate. The centerline velocity results showed an over-prediction of the core length by approximately 4 to 5 nozzle diameters. RANS results obtained by Georgiadis et al. [29] for a $M_j = 0.513$ and TTR = 1.00 jet, also show an over-prediction of the core length by approximately 3 nozzle diameters when closed by the Mentor-SST turbulence model. The radial velocity profile at $xD^{-1} = 4$ agrees well with experimental measurements. The radial TKE profile at $xD^{-1} = 4$ shows a slight over-prediction of TKE in the shear layer from $0.45 < rD^{-1} < 7$.

B. Refraction Effects

An attempt to account for the effects of refraction on the sound spectrum at the far-field observer location is made by implementing the high-frequency asymptotic Green's function solution to Lilley's equation obtained by Balsa [18] and Wundrow and Khavaran [19]. The modified Green's function of Eqn. 29 is obtained analytically by assuming that terms scaling like $1/r_s$ are dominant and azimuthal derivatives can be neglected. This result is compared to the free-space Green's function $\mathcal{G}_0$. From the results (Fig. 4), $\mathcal{G}_q$ appears to more accurately capture the fine-scale noise spectrum at high frequencies. Figure 4 indicates that the quasi-symmetric Green's function of Wundrow and Khavaran [19] and Balsa [18] when implemented in a spectral density prediction equation with the source term of Tam and Auriault [8] can account for some of the refraction effects of the jet shear layer. Further improvements to these predictions can be made by considering the asymmetric Green's function of Wundrow and Khavaran [19] or the Green's function solution of Khavaran [30].

C. Shielding Predictions

In this paper, it is proposed that G_f in both $\mathcal{G}_0$ and $\mathcal{G}_q$ can be replaced with the tailored Green's function solution of Ffowcs Williams and Hall [17] to account for the scattering effects of a semi-infinite plate. Figures 5 and 6 investigate the ability of $\mathcal{G}_0$ and $\mathcal{G}_q$ to capture the scattering effects of a semi-infinite flat plate at $xD^{-1} = 15$ and $rD^{-1} = 16$ with a jet operating at setpoint 7. At angles upstream of $\theta = 100°$, $\mathcal{G}_q$ predicts more precisely the change in decibels ΔdB at higher frequencies than $\mathcal{G}_0$. For angles downstream of $\theta = 100°$, $\mathcal{G}_0$ shows improved predictions of ΔdB. This is attributed to the formulation of the shielded Green's functions. An exact solution for Lilley's equation when a semi-infinite flat plate is in the far-field will be required for greater accuracy of $\mathcal{G}_q$.

V. Appendix

A. Derivation of Pressure Solution

The integral in Eqn. 12 will now be re-arranged into a more convenient form. We start by considering the source term Λ. Λ can be re-arranged to the following form in a cylindrical coordinate system,

$$\frac{D}{Dt}\nabla\cdot\overline{c}^2\nabla q_s = \nabla\cdot\overline{c}^2\nabla\frac{Dq_s}{Dt} - \left[\frac{1}{r}\frac{\partial}{\partial r}\left(r\overline{c}^2\frac{\partial\overline{u}}{\partial r}\frac{\partial q_s}{\partial x}\right) + \overline{c}^2\frac{\partial\overline{u}}{\partial r}\frac{\partial^2 q_s}{\partial r\partial x}\right]. \tag{57}$$

The convolution integral of the first term in Eqn. 57 with the Green's function can be rearrange by making use of Green's second identity,

$$\int_{-\infty}^{\infty}\int_{-\infty}^{\infty}\int_{-\infty}^{\infty} g(\mathbf{x},t|\mathbf{x}_s,t_s)\nabla\cdot\overline{c}^2\nabla\frac{Dq_s}{Dt}d\mathbf{x} = \oiint_S \overline{c}^2\left(g\frac{\partial}{\partial\mathbf{n}}\left(\frac{Dq_s}{Dt}\right) - \frac{Dq_s}{Dt}\frac{\partial g}{\partial\mathbf{n}}\right)dS + \int_{-\infty}^{\infty}\int_{-\infty}^{\infty}\int_{-\infty}^{\infty}\nabla\cdot\overline{c}^2\nabla g\frac{Dq_s}{Dt}d\mathbf{x}. \tag{58}$$

The surface integral can be evaluated beyond the jet boundary, where $q = 0$, and thus becomes negligible. The convolution integral of g with the remaining term of Eqn. 57 can be easily rearranged using integration by parts. The resulting expression for the pressure solution becomes,

$$p(\mathbf{x},t) = \int_{-\infty}^{\infty}\cdots\int_{-\infty}^{\infty}\frac{Dq_s}{Dt_s}\nabla_s\cdot\overline{c}_s^2\nabla_s g + \left[\frac{\partial g}{\partial x_s}\frac{1}{r_s}\frac{\partial}{\partial r_s}\left(r\overline{c}_s^2\frac{\partial\overline{u}_s}{\partial r_s}\right) - \frac{\partial}{\partial r_s}\left(\overline{c}_s^2\frac{\partial\overline{u}_s}{\partial r_s}\frac{\partial g}{\partial x_s}\right)\right]q_s d\mathbf{x}_s dt_s. \tag{59}$$

Acknowledgements

The first author is supported by the University of Florida Herbert Wertheim College of Engineering Graduate School Preeminence Award. The first author would like to acknowledge the Herbert Wertheim College of Engineering and the Mechanical and Aerospace Engineering Department at the University of Florida for supporting this research.

References

[1] Balsa, T., Gliebe, P., Kantola, R., Mani, R., Stringas, E., and Wang, J., "High Velocity Jet Noise Source Location and Reduction," Technical Report FAA-RD-76-79, General Electric Company, May 1978. URL https://apps.dtic.mil/docs/citations/ADA094291.

[2] Wang, M. E., "Wing Effect on Jet Noise Propagation," *Journal of Aircraft*, Vol. 18, No. 4, 1981, pp. 295–302. doi:10.2514/3.57493, URL https://doi.org/10.2514/3.57493.

[3] Brown, C., "Jet-Surface Interaction Test: Far-Field Noise Results," *Volume 1: Aircraft Engine, Ceramics, Coal, Biomass and Alternative Fuels, Controls, Diagnostics and Instrumentation*, ASME, 2012. doi:10.1115/gt2012-69639, URL https://doi.org/10.1115/gt2012-69639.

[4] Khavaran, A., Krejsa, E. A., and Kim, C. M., "Computation of Supersonic Jet Mixing Noise for an Axisymmetric Convergent-Divergent Nozzle," *Journal of Aircraft*, Vol. 31, No. 3, 1994, pp. 603–609. doi:10.2514/3.46537, URL https://doi.org/10.2514/3.46537.

[5] Zhao, W., Frankel, S. H., and Mongeau, L., "Large Eddy Simulations of Sound Radiation from Subsonic Turbulent Jets," *AIAA Journal*, Vol. 39, No. 8, 2001, pp. 1469–1477. doi:10.2514/2.1497, URL https://doi.org/10.2514/2.1497.

[6] Khalighi, Y., Ham, F., Nichols, J., Lele, S., and Moin, P., "Unstructured Large Eddy Simulation for Prediction of Noise Issued from Turbulent Jets in Various Configurations," *17th AIAA/CEAS Aeroacoustics Conference (32nd AIAA Aeroacoustics Conference)*, American Institute of Aeronautics and Astronautics, AIAA 2011-2886, 2011. doi:10.2514/6.2011-2886, URL https://doi.org/10.2514/6.2011-2886.

[7] Ffowcs Williams, J. E., and Hawkings, D. L., "Sound Generation by Turbulence and Surfaces in Arbitrary Motion," *Philosophical Transactions of the Royal Society A: Mathematical, Physical and Engineering Sciences*, Vol. 264, No. 1151, 1969, pp. 321–342. doi:10.1098/rsta.1969.0031, URL https://doi.org/10.1098/rsta.1969.0031.

[8] Tam, C. K. W., and Auriault, L., "Jet Mixing Noise from Fine-Scale Turbulence," *AIAA Journal*, Vol. 37, No. 2, 1999, pp. 145–153. doi:10.2514/2.691, URL https://doi.org/10.2514/2.691.

[9] Morris, P. J., and Farassat, F., "Acoustic Analogy and Alternative Theories for Jet Noise Prediction," *AIAA Journal*, Vol. 40, No. 4, 2002, pp. 671–680. doi:10.2514/2.1699, URL https://doi.org/10.2514/2.1699.

[10] Smith, M. J., and Miller, S. A. E., "The Effects of Surfaces on the Aerodynamics and Acoustics of Jet Flows," *19th AIAA/CEAS Aeroacoustics Conference*, American Institute of Aeronautics and Astronautics, AIAA 2013-2041, 2013. doi:10.2514/6.2013-2041, URL https://doi.org/10.2514/6.2013-2041.

[11] Miller, S. A. E., "The Prediction of Jet Noise Ground Effects using an Acoustic Analogy and a Tailored Green's Function," *Journal of Sound and Vibration*, Vol. 333, No. 4, 2014, pp. 1193–1207. doi:10.1016/j.jsv.2013.10.028, URL https://doi.org/10.1016/j.jsv.2013.10.028.

[12] Miller, S. A. E., "The Prediction and Analysis of Jet Flows and Scattered Turbulent Mixing Noise about Flight Vehicle Airframes," Tech. Rep. NASA/TM-2014-218506, 2014. URL https://ntrs.nasa.gov/archive/nasa/casi.ntrs.nasa.gov/20140010739.pdf.

[13] Papamoschou, D., "Prediction of Jet Noise Shielding," *48th AIAA Aerospace Sciences Meeting Including the New Horizons Forum and Aerospace Exposition*, American Institute of Aeronautics and Astronautics, AIAA 2010-653, 2010. doi:10.2514/6.2010-653, URL https://doi.org/10.2514/6.2010-653.

[14] Liu, Y., *Fast Multipole Boundary Element Method - Theory and Applications in Engineering*, Cambridge University Press, 2009.

[15] Lilley, G., "On The Noise from Jets, Noise Mechanisms," *AGARD-CP-131*, 1974, pp. 13.1–13.12.

[16] Brown, C., and Bridges, J., "Small Hot Jet Acoustic Rig Validation," Tech. Rep. 20060013451, NASA Glenn Research Center, apr 2006. URL https://ntrs.nasa.gov/archive/nasa/casi.ntrs.nasa.gov/20060013451.pdf.

[17] Ffowcs Williams, J. E., and Hall, L. H., "Aerodynamic Sound Generation by Turbulent Flow in the Vicinity of a Scattering Half Plane," *Journal of Fluid Mechanics*, Vol. 40, No. 04, 1970, p. 657. doi:10.1017/s0022112070000368, URL https://doi.org/10.1017/s0022112070000368.

[18] Balsa, T. F., "The Far Field of High Frequency Convected Singularities in Sheared Flows, with an Application to Jet-Noise Prediction," *Journal of Fluid Mechanics*, Vol. 74, No. 2, 1976, pp. 193–208. doi:10.1017/s0022112076001766, URL https://doi.org/10.1017/s0022112076001766.

[19] Wundrow, D. W., and Khavaran, A., "On the Applicability of High-Frequency Approximations to Lilley's Equation," *Journal of Sound and Vibration*, Vol. 272, No. 3-5, 2004, pp. 793–830. doi:10.1016/s0022-460x(03)00420-6, URL https://doi.org/10.1016/s0022-460x(03)00420-6.

[20] Lighthill, M. J., "On Sound Generated Aerodynamically I. General theory," *Proceedings of the Royal Society of London. Series A. Mathematical and Physical Sciences*, Vol. 211, No. 1107, 1952, pp. 564–587. doi:10.1098/rspa.1952.0060, URL https://doi.org/10.1098/rspa.1952.0060.

[21] Boussinesq, J., "Théorie des Ondes et des Remous qui se Propagent le Long d'un Canal Rectangulaire Horizontal, en Communiquant au Liquide Contenu dans ce canal des Vitesses Sensiblement Pareilles de la Surface au Fond." *Journal de Mathématiques Pures et Appliquées*, 1872, pp. 55–108. URL http://eudml.org/doc/234248.

[22] Khintchine, A., "Korrelations Theorie der Stationären Stochastischen Prozesse," *Mathematische Annalen*, Vol. 109, No. 1, 1934, pp. 604–615. doi:10.1007/BF01449156, URL https://doi.org/10.1007/BF01449156.

[23] Thies, A. T., and Tam, C. K. W., "Computation of Turbulent Axisymmetric and Nonaxisymmetric Jet Flows using the k-epsilon Model," *AIAA Journal*, Vol. 34, No. 2, 1996, pp. 309–316. doi:10.2514/3.13065, URL https://doi.org/10.2514/3.13065.

[24] Mentor, F. R., "Improved Two-Equation k-ω Turbulence Models for Aerodynamic Flows," Technical Report NASA-TM-103975, A-92183, NAS 1.15:103975, NASA Ames Research Center, Oct 1992. URL http://hdl.handle.net/2060/19930013620.

[25] Goldstein, M. E., *Aeroacoustics*, McGraw-Hill International Book Co, 1976. URL https://www.xarg.org/ref/a/0070236852/.

[26] Zhang, S., Jin, J., and Crandall, R. E., "Computation of Special Functions," *American Journal of Physics*, Vol. 65, No. 4, 1997, pp. 355–355. doi:10.1119/1.18543, URL https://doi.org/10.1119/1.18543.

[27] *Simcenter STAR-CCM+ Documentation*, Siemens PLM Software, 2018.

[28] Bridges, J., and Wernet, M. P., "The NASA Subsonic Particle Image Velocimetry (PIV) Dataset," Technical Report NASA/TM-2011-216807, NASA Glenn Research Center, Nov 2011. URL http://hdl.handle.net/2060/20110023688.

[29] Georgiadis, N. J., Yoder, D. A., and Engblom, W. B., "Evaluation of Modified Two-Equation Turbulence Models for Jet Flow Predictions," *AIAA Journal*, Vol. 44, No. 12, 2006, pp. 3107–3114. doi:10.2514/1.22650, URL https://doi.org/10.2514/1.22650.

[30] Khavaran, A., "Exhaust Noise Green's Function in Turbofan Jet Engines with an External Centerbody," *AIAA Journal*, 2019, pp. 1–16. doi:10.2514/1.j057723, URL https://doi.org/10.2514/1.j057723.